coatings

MDPI

Article

Corrosion Resistance of Anodic Layers Grown on 304L Stainless Steel at Different Anodizing Times and Stirring Speeds

Laura Patricia Domínguez-Jaimes [1], María Ángeles Arenas Vara [2], Erika Iveth Cedillo-González [1], Juan Jacobo Ruiz Valdés [1], Juan José De Damborenea [2], Ana Conde Del Campo [2], Francisco Javier Rodríguez-Varela [3], Ivonne Liliana Alonso-Lemus [4] and Juan Manuel Hernández-López [1,*]

1 Universidad Autónoma de Nuevo León, Facultad de Ciencias Químicas, Ciudad Universitaria, Av. Universidad s/n., Nuevo León C. P. 66455, Mexico; lauradominguez288@gmail.com (L.P.D.-J.); erika.cedillogn@uanl.edu.mx (E.I.C.-G.); juan.ruizv@uanl.mx (J.J.R.V.)
2 Department of Surface Engineering Corrosion and Durability, National Center for Metallurgical Research, CENIM-CSIC, Avda. Gregorio del Amo, 8, 28040 Madrid, Spain; geles@cenim.csic.es (M.Á.A.V.); jdambo@cenim.csic.es (J.J.D.D.); a.conde@cenim.csic.es (A.C.D.C.)
3 Sustentabilidad de los Recursos Naturales y Energía, Cinvestav Unidad Saltillo, Av. Industria Metalúrgica, 1062, Ramos Arizpe 25900, Coahuila, Mexico; javier.varela@cinvestav.edu.mx
4 Conacyt, Cinvestav Unidad Saltillo. Av. Industria Metalúrgica 1062, Ramos Arizpe 25900, Coahuila, Mexico; ivonne.alonso@cinvestav.edu.mx
* Correspondence: hljmanuel@gmail.com or juan.hernandezlz@uanl.edu.mx; Tel.: +52-1-55-11941410

Received: 30 September 2019; Accepted: 25 October 2019; Published: 29 October 2019

Abstract: Different chemical and physical treatments have been used to improve the properties and functionalities of steels. Anodizing is one of the most promising treatments, due to its versatility and easy industrial implementation. It allows the growth of nanoestructured oxide films with interesting properties able to be employed in different industrial sectors. The present work studies the influence of the anodizing time (15, 30, 45 and 60 min), as well as the stirring speed (0, 200, 400, and 600 rpm), on the morphology and the corrosion resistance of the anodic layers grown in 304L stainless steel. The anodic layers were characterized morphologically, compositionally, and electrochemically, in order to determine the influence of the anodization parameters on their corrosion behavior in a 0.6 mol L^{-1} NaCl solution. The results show that at 45 and 60 min anodizing times, the formation of two microstructures is favored, associated with the collapse of the nanoporous structures at the metal-oxide interphace. However, both the stirring speed and the anodizing time have a negligeable effect on the corrosion behavior of the anodized 304L SS samples, since their electrochemical values are similar to those of the non-anodized ones.

Keywords: anodization; stainless steel; anodic layer; corrosion resistance

1. Introduction

In recent years, surface engineering has developed physical, chemical, mechanical, and microstructural modification treatments on steel to expand the range of applications. Literature is quite extensive about the surface treatments carried out to date [1–6]. Nevertheless, the anodizing process that was initially developed for aluminum alloys [7,8] and later for other metals, such as Mg [9], Ga [10], Co [11], W [12], Nb [13], Zr [14], Sn [15], and Ti [16,17], has emerged as a new alternative to surface functionalization of iron base alloys of particular interest in fields such as photocatalysis, sensors, corrosion, environmental remediation, and biomedical to name a few [18–30].

In photocatalysis applications, anodic layers have been considered an adequate way to achieve greater efficiency due to the increase in surface area. First studies about semiconducting properties and growth of nanostructured layers on ferrous materials were reported by Prakasam et al. [31] who achieved thicknesses of 300–600 nm and pore diameters from 50 to 250 nm on iron. Further, Zhang et al. have explored the photocatalytic decomposition of methylene blue [19] and the degradation of azo dye [20] by anodic iron oxides in different nanostructures.

Likewise, the nanostructures growth on iron and its alloys is quite promising for water splitting reaction under solar or visible-light illumination [23,24]. Rangaraju et al. [25] studied different nanostructure configurations of photoanodes based on anodic iron oxide for photoelectrochemical water oxidation. These authors obtained better photocatalytic properties in 1 mol L^{-1} KOH with Air mass 1.5 Global light illumination when the photoanode has a two-layered oxide structure comprised by a top layer with nano-dendrite morphology and a bottom layer of nanoporous morphology. Moreover, these authors state that layer close to the metal provide corrosion resistance compared with the top layer [26].

On the other hand, in terms of biomedical applications, Asoh et al. [29] reported the growth of anodic layers on type 304 stainless steel in an anodizing bath of hydrogen peroxide and sulfuric acid is suitable to prepare the surface prior to the deposit of synthetic bioactive hydroxyapatite in biomedical implant devices. However, even though corrosion resistance is an important issue in medical devices and applications [32,33], literature is scarce in the electrochemical characterization of anodic layers on stainless steel.

The range of applications and properties, which can be tailored and improved by manipulating the nanostructure is wide. As the morphology and structural characteristics of the anodic layers are deeply correlated with the anodizing conditions, the control of the anodizing parameters such as potential applied, temperature, electrolyte composition and anodizing time is key to the formation of the nanoestructure of the anodic layers [18,34–36].

Various researchers have studied the growth of anodic layers on stainless steels, being 316L [25,26] and 304 [27–30] the most commonly used. The studies on 316L SS indicate that the addition of water to organic baths improves the diameter and thickness of the grown layers [37]. On the other hand, the use of fluoride-free solutions enables to obtain anodic layers composed of a mixture of hydroxides-oxides-sulfates [38].

Literature reporting the growth of anodic layers on stainless steel 304 preferentially use a mixture of glycerol or ethylene glycol and NH_4F and different additions of H_2O as organic anodizing bath. Theresearch performed in these media allowed concluiding three main aspects: (1) the anodic layers have similar Fe, Cr, Ni contents to the substrate [39], (2) the concentration of H_2O concentration in the anodizing bath determines the morphological characteristics of the anodic layers [40] and (3) the voltage applied favored different growth mechanisms leading to the fabricationof anodic layers with different chemical compositions [29].

Nevertheless, most of the existing works so far are focused on the growth and chemical/ morphological characterization of the anodic layers on these ferrous materials [29,35,39–42], but not on their influence on the electrochemical response or corrosion resistance properties. For that reason, the objective of this work is to explore the corrosion properties in a NaCl solution of the anodic layers grown on 304L SS at different stirring speeds and anodizing times inthylene glycol with 0.1 mol L^{-1} NH_4F and 0.1 mol L^{-1} H_2O.

2. Materials and Methods

Disks of diameter 22.2mm of 304L SS (18.3 wt.% Cr, 8.11 wt.% Ni, 1.52 wt.% Mn, 0.27 wt.% Si) supplied by Jay Steel Corporation, Mumbai, India, were ground using successive grades of SiC paper up to 2000 grade, degreased with detergent and rinsed with tap water followed by deionized water.

Anodic layers were formed in a two-electrode cell by anodizing the 304L SS substrates at constant voltage at 50 V in ethylene glycol electrolyte containing 0.1 mol L^{-1} NH_4F and 0.1 mol L^{-1} H_2O for 15, 30, 45 and 60 min at a constant temperature of 5 °C, under stirring conditions at 0, 200, 400 and 600 rpm. Finally, a platinum mesh was used as a cathode.

Plan view morphology of the anodic oxide films was examined by field emission gun scanning electron microscopy (FEG–SEM) utilizing Hitachi 4800 instrument (Tokyo, Japan) equipped with Energy Dispersive X-ray Spectroscopy (EDX) facilities, operated at 15 keV for EDX analysis and 7 keV for secondary electron imaging. Each of the areas and local EDX analysis results are quoted as an average of 3 measurements.

The electrochemical measurements were done in triplicate in a conventional three-electrode cell. The working electrodes were either the non-anodized or anodized samples, an Ag/AgCl electrode (3 mol L^{-1} KCl), was used as reference electrode and the counter electrode was a platinum wire. The solution to evaluate the corrosion properties was a 0.6 mol L^{-1} NaCl at room temperature. Corrosion behavior was evaluated by potentiodynamic polarization using a Gamry Reference 600 potentiostat. The potentiodynamic curves were conducted at a scan rate of 0.16 mV/s. Before starting the scan, the sample remained in the solution for 15 min to stabilize the open circuit potential (OCP). The potential scan was started in the anodic direction from a potential value of 0.3 V with respect to the OCP to 1 V with respect to the Ag/AgCl electrode or when the sample reached a current density of 0.5 A/cm^2. Electrochemical Impedance Spectroscopy (EIS) measurement were performed in a VSP-300 Biologic potentiostat, applying a sinusoidal signal of 10 mV peak to peak of amplitude vs. OCP. The frequency range was from 100 kHz to 100 mHz and recording 10 points per decade. Measurements were carried out at 0 and 24 h of immersion. The experimental data were analyzed using the ZVIEW software (v. 3.1c).

3. Results and Discussion

3.1. Influence of Stirring Speed on the Growth of Anodic Layers

To investigate the effect of the stirring speed on the growth of the anodic layers, the anodizing processes were carried out at four different stirring speeds (0, 200, 400, and 600 rpm). Figure 1 plots the current density versus time recorded during the anodizing processes performed at different stirring speeds. The shape of the anodizing curve is characteristic of the growth of of porous anodic layers reported for different valve metals [19,43–45] and it comprises three stages: (I) an abrupt decrease in the current density during the first seconds of the anodizing process related to the growth of a dense oxide film on the surface of the metal known as barrier layer, (II) a gradual increase of the current density related to preferential dissolution zones randomly distributed on the surface of the barrier layer, which corresponds to the nucleation of the pores and (III) a step of stable current density related to the coarsening of the anodic layer [46].

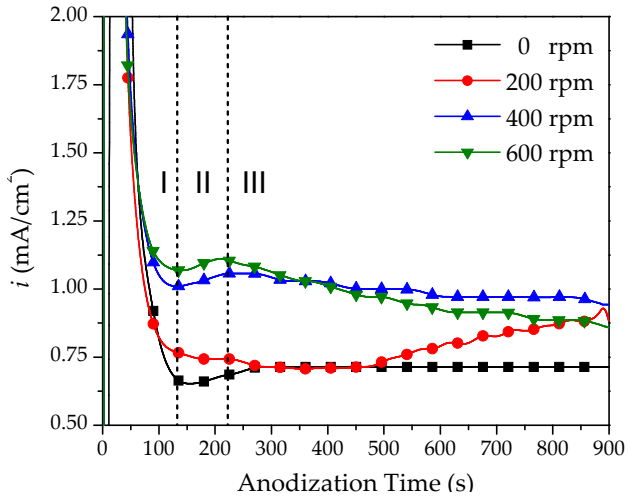

Figure 1. Current density–time responses for anodizing on 304L SS for 15 min in ethylene glycol-NH_4F-H_2O electrolyte at different stirring speeds.

Moreover, the charge density estimated by integrating the current density-time responses depends on the stirring speed. The charge density that passes through the system during the anodizing treatments performed for 15 min varies from ~0.750, ~0.864, ~1.027, and ~1.061 C/cm^2, for 0, 200, 400, and 600 rpm, respectively. This higher current density (charge density), observed for higher stirring rates (400, 600 rpm) points out to an enhanced transport of ionic species from the solution to the metal/electrolyte interface and, therefore, to the enhancement of the chemical dissolution mechanism as it has been reported in literature [47,48].

The electrochemical response was studied by polarization curves in 0.6 mol L^{-1} NaCl solution, Figure 2. The non-anodized 304L SS samples present a corrosion potential (E_{corr}) of ~−244.9 mV, a pitting potential (E_{pit}) of ~441.6 mV, and a passive current density (i_{pass}) of about 8.3×10^{-7} A/cm^2. The anodic layers obtained at different stirring speeds showed an electrochemical response similar to the non-anodized samples, characterized by E_{corr} values ranging about −312.1 mV and i_{pass} of about 4.10×10^{-7} A/cm^2. However, the pitting potential E_{pit} shifts toward lower values, about ~329.5 mV for the anodic layers grown at 0, 200 and 400 rpm. While, for the oxide layer grown at 600 rpm showed the lowest pitting potential, ~140.5 mV, indicating that it is the most prone to localized corrosion.

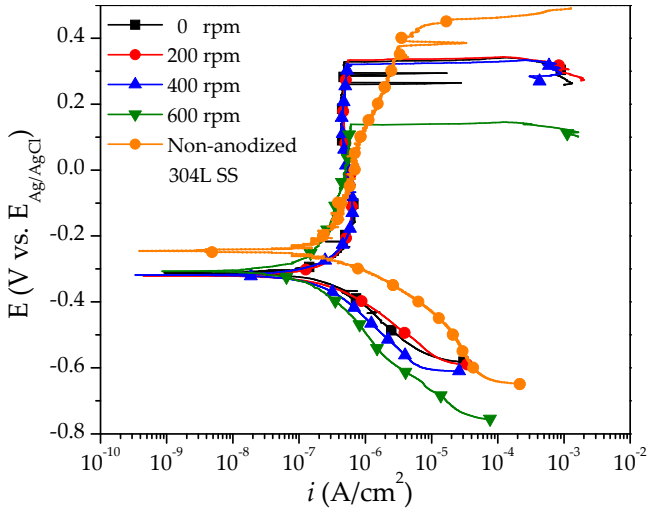

Figure 2. Potentiodynamic polarization curves of the samples anodized for 15 min, at different stirring speeds.

3.2. *Influence of Anodizing Time on the Growth of Anodic Layers*

Figure 3 shows the current density-time curves recorded during the anodizing treatments at 0 rpm and at 600 rpm for different anodizing times (15, 30, 45, 60 min). The three steps described in Figure 1 for the anodizing process developed for 15 min at different stirring speeds are observed but, the length of each one varies significantly with the stirring speed.

As it shows in Figure 3a, the first stage associated with the formation of the barrier layer occurs up to 500 s for the anodizing performed at 0 rpm, while at 600 rpm (Figure 3b) it is shorter, about 200 s. This difference indicates that the barrier layer grows faster under stirring conditions due to the mass transfer is favored under stirring conditions. Moreover, higher current densities were also observed during the anodization performed at 600 rpm. The current increase is also reflected in the charge density, which is about 4 times higher at 600 rpm than at 0 rpm for a specific anodizing time. It varies from ~0.710 to ~3.626 C/cm^2 for 0 rpm and from ~1.631 to ~4.438 C/cm^2 for 600 rpm, Figure 3c.

From the charge density values, the theoretical thickness of the anodic layer can be estimated assuming that the entire charge is used for the formation of FeOOH, acoording to Equation (1) This

compound has been previously reported as the main component of the anodic layers grown in ferrous materials [35,41,49].

$$Anodic\ layer\ thickness = Q\left[\frac{C}{cm^2}\right] * \frac{Mw_{FeOOH}}{nF\rho_{\ FeOOH}}\left[\frac{cm^3}{C}\right] \quad (1)$$

where Q is the charge density of the current density–time plot, Mw is the molecular weight ρ is the density, n is the number of electrons equivalent and F is the Faraday constant.

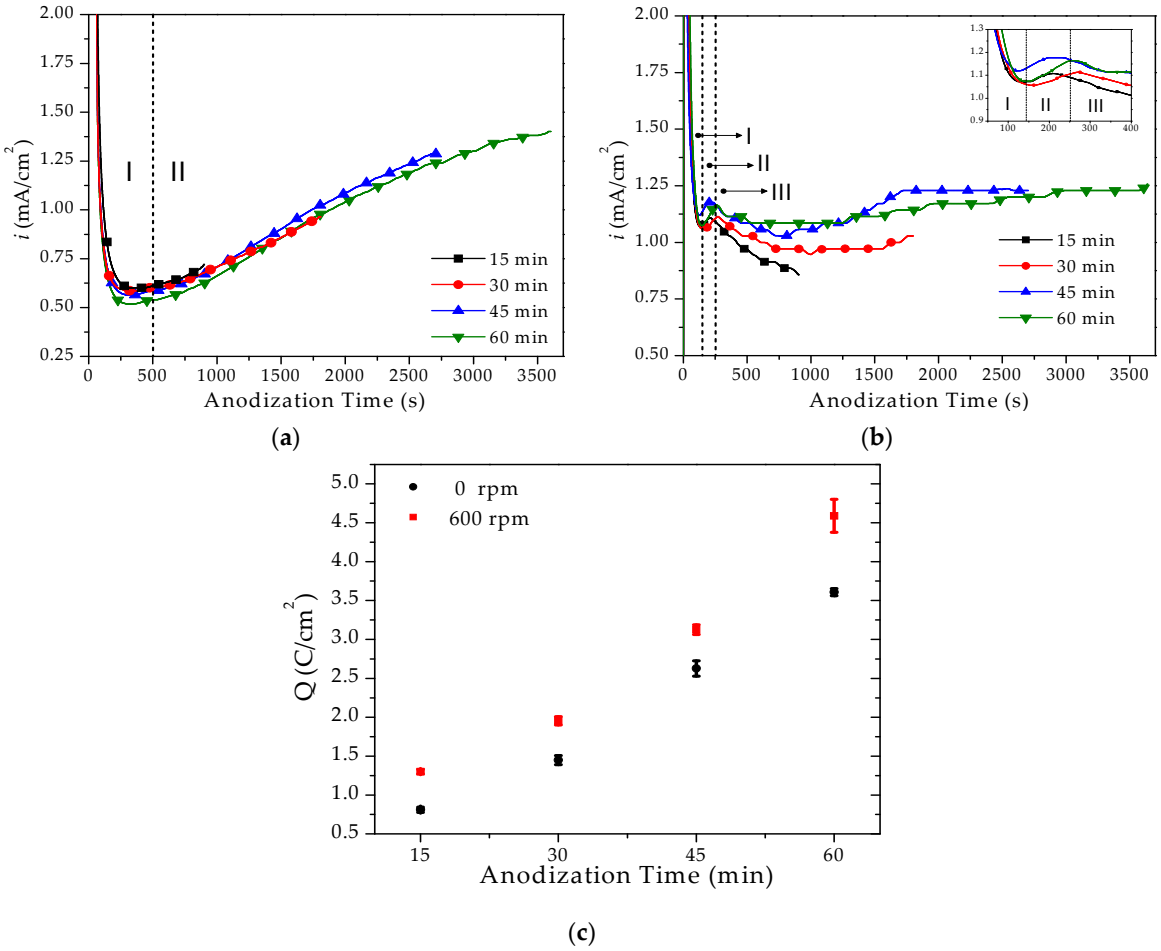

Figure 3. Current density–time responses for anodizing on 304L SS in ethylene glycol-NH_4F-H_2O electrolyte for different anodizing time at (**a**) 0 rpm; (**b**) 600 rpm stirring speeds. (**c**) Charge density obteined of current density-time plots at 0 and 600 rpm.

The thicknesses estimated for the anodic layers grown at 0 rpm and different anodizing times are: 581 nm (15 min), 1.07 µm (30 min), 1.83 µm (45 min) and 2.60 µm (60 min). For the layers grown at 600 rpm the thickness obtained for different anodizing times are: 739 nm (15 min), 1.43 µm (30 min), 2.27 µm (45 min) and 3.18 µm (60 min) at 600 rpm. These results suggest that the higher the anodizing time and stirring speed, the thicker the anodic layers; however, this simplistic analysis does not take into account the chemical dissolution and dissolution assisted by the electric field processes involved during the fabrication of the anodic layers. Both processes compete with the growth mechanism resulting an anodic oxide layers with lower thickness [42,50]. As can be seen in Figure 4, where the anodic layers generated for 15 and 60 min at 0 rpm show thicknesses around 500 and 1400 nm, respectively, these values being lower than those obtained theoretically.

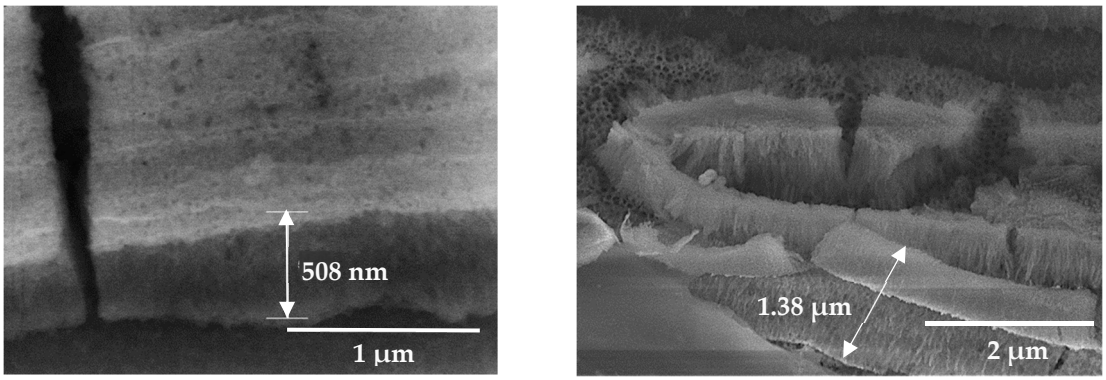

(**a**) (**b**)

Figure 4. SEM images of anodic layer thickness grown in ethylene glycol-NH_4F-H_2O electrolyte for (**a**) 15 min and (**b**) 60 min at 0 rpm.

Figure 5 shows the morphology of the anodic layers grown during different anodizing times 15–60 min at 0 rpm and 60 min at 600 rpm. The anodized layers grown for 15 min show a surface covered with a uniform oxide layer which reproduces the topography of the surface finish. At higher magnifications this surface shows nanoporous morphology due to the distribution of the electric field in the anodic layer, Figure 5a,b. For 30 min of anodizing time the anodic oxide layer shows a similar appearance. At higher magnifications the nanoporous mophology of the anodic layer is observed, Figure 5c,d. The samples anodized for 45 min shows a notably different surface appearance whith two zones clearly distinguished. A lighter Zone 1 with elongated shape appearance deposited on top a darker area (Zone 2). At higher magnifications de Zone 2 still keeps the nanoporous morphology observed at shorter anodizing times although with higher distribution in pore diameter, Figure 5e,f. The increase of anodizing time to 60 min enhances the features observed in the previous images Figure 5g–j. It looks like there is a coarsening of the whiter areas (Zone 1), which become closer one to others. As results the top view of the surface shows a narrowing of the darker areas (Zone 2), Figure 5g,h. On the other hand, the samples grown for 60 min at 600 rpm, show a cleaner anodic surface, than those obtained at the same time at 0 rpm, Figure 5i,j. This is associated with a higher mass transfer and a constant elimination of matter during anodizing due to stirring speed. Despite to the anodic oxid film appears lo collapse for longer anodizing times, the anodic layer placed underneath remains adhered to the substrate and keeps an ordered nanoporous morphology.

These results reveal that the anodizing time influences both the morphology and the pore diameter, obtaining values of 42.56 ± 5.03 for 15 min and 63.0 ± 11.0 nm for 60 min of anodizing at 0 rpm and values of 65.97 ± 10.53 nm for 60 min of anodizing at 600 rpm.

On the other hand, Table 1 shows the results of Energy Dispersive X-ray Spectroscopy (EDX) analysis for anodic layer obtained at 0 rpm for different time of treatment. The distribution of the elements is analyzed in two zones: Zone 1 corresponds to the outer layer located at the oxide/electrolyte interface; and Zone 2 corresponds to the nanoporous layer placed underneath that is observed after 45 min of treatment. Both zones show a similar trend since the content of F and O elemental increases while the percentage of other elements such as Cr, Fe, and Ni tends to decrease with the anodizing time. The above is caused by a fluorine and oxygen incorporation from the electrolyte, which likely leads to the formation of fluoride compounds, mainly FeF_2, FeF_3, and FeOOH [40,49]. Nevertheless, at 45 min of treatment, F values decrease abruptly from 44.50 at.% to 16.41 at.% and O values from 11.66 at.% to 5.64 at.% between Zone 1 and Zone 2, respectively.

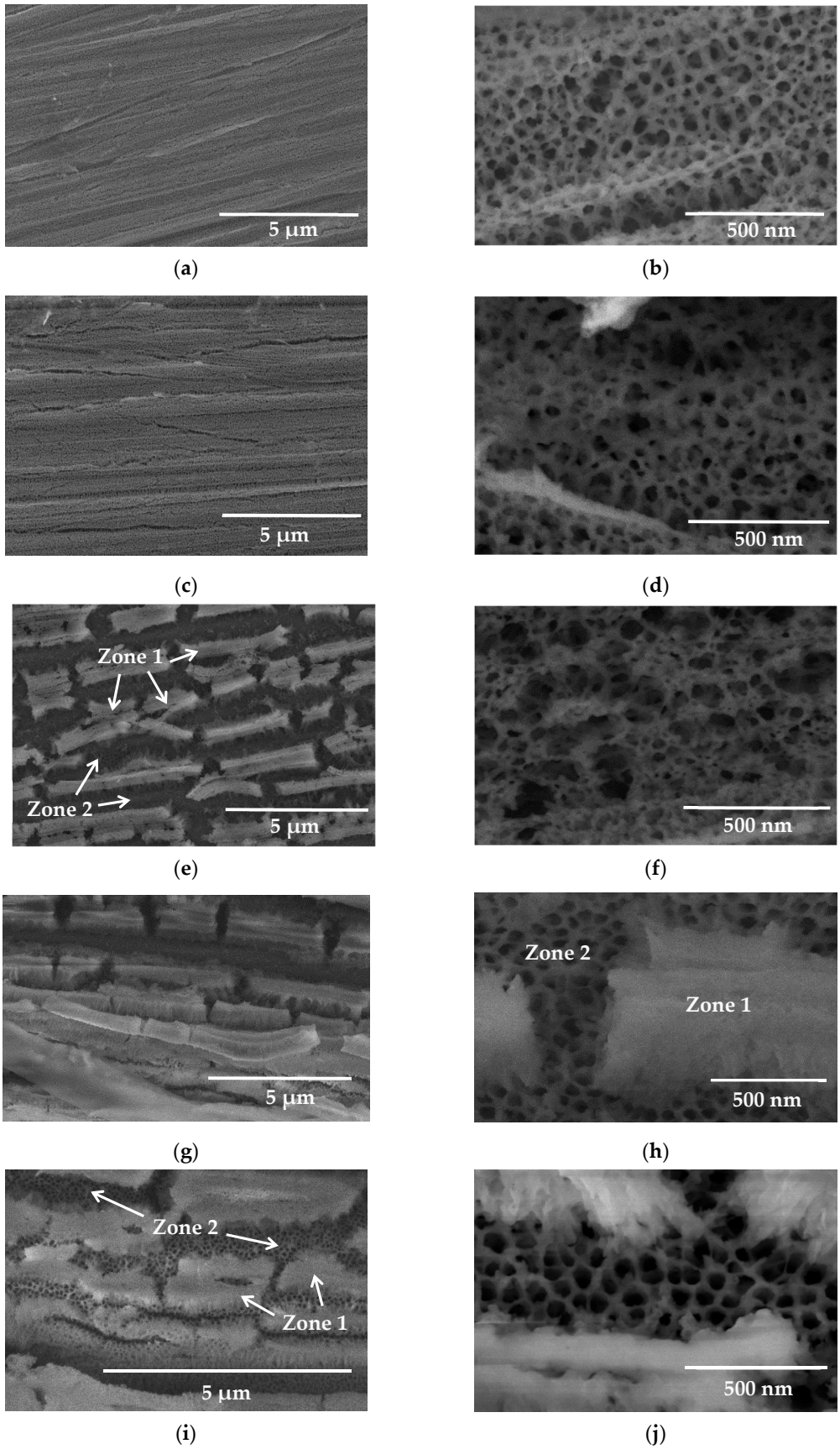

Figure 5. SEM images of anodic layers grown in ethylene glycol-NH_4F-H_2O electrolyte at 0 rpm for (**a**,**b**) 15 min; (**c**,**d**) 30 min; (**e**,**f**) 45 min; (**g**,**h**) 60 min; and (**i**,**j**) 60 min at 600 rpm.

Table 1. Energy Dispersive X-ray Spectroscopy (EDX) results for the anodic layers grown at different anodizing times at 0 rpm.

Element, at. %		C	O	F	Cr	Mn	Fe	Ni
Anodization time (min)	15	5.15 ± 0.86	5.95± 0.79	35.61 ± 3.42	11.53 ± 0.80	0.51 ± 0.20	37.17 ± 3.04	4.08 ± 0.63
	30	4.88 ± 0.97	9.33 ± 1.85	41.42 ± 7.60	9.92 ± 1.61	0.56 ± 0.23	30.80 ± 6.37	3.08 ± 0.72
	45 Zone 1	4.18 ± 1.81	11.66 ± 1.13	44.50 ± 10.31	9.82 ± 1.85	0.40 ± 0.22	27.20 ± 7.89	2.25 ± 0.85
	45 Zone 2	5.50 ± 1.26	5.64 ± 0.69	16.41 ± 1.05	15.59 ± 0.56	0.72 ± 0.22	50.72 ± 1.24	5.42 ± 0.35
	60 Zone 1	3.18 ± 0.34	22.74 ± 2.97	59.06 ± 11.56	5.69 ± 0.98	0.34 ± 0.26	8.67 ± 1.20	0.32 ± 0.19
	60 Zone 2	8.70 ± 2.57	5.21 ±1.03	16.54 ± 1.81	14.39 ± 0.83	1.34 ± 1.48	47.77 ± 2.42	6.05 ± 0.97

The corrosion behavior of the anodic layers at 0 rpm is shown in Figure 6. The polarization curve for the anodizing at 15 min shows a passive region similar to the non-anodized 304L SS but broader compared to the other treatments. The E_{corr} of the sample treated at 15 min is ~−322.8 mV, while for the other anodizing times this potential shifts towards nobler values up to ~−57.3 mV. However, all the anodizing treatments show a i_{pass} about ~5.4×10^{-7} A/cm^2 and a E_{pit} of ~281.3 mV indicating a similar corrosion kinetics than the non-anodized samples but higher susceptibility to localized corrosion. Performing a thermal treatment could be an interesting alternative to improve the electrochemical response of the oxide layers since it allows the obtaining more stable oxides and the elimination of fluoride inside the anodic layers, as has been reported of Titanium and its alloys [51].

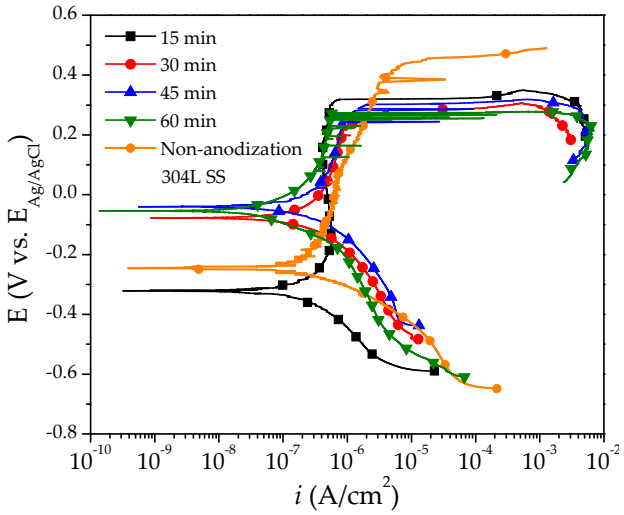

Figure 6. Potentiodynamic polarization curves of the samples anodized for different anodizing times at 0 rpm.

3.3. Electrochemical Spectroscopy Impedance

Figure 7 shows the electrochemical impedance spectra at different immersion times 0 and 24 h, for both non-anodized and anodized samples at different immersion times and stirring speeds.

Figure 7a,b, shows the evolution with time of impedance corresponding to the non-anodized sample. The response is comprised by a single time constant at both immersion times. The /Z/ plot shows a linear stage in a wide frequency range with a slope of ~−1 and a phase angle of about 80° pointing out to a capacitive behavior or blocking electrode. This behavior is characteristic of passive metals covered with a native oxide layer. The slight deviation observed at the Bode plots at low frequencies is related to the surface finish of the sample and the quality of the native oxide layer that grows on it [52–54].

In the same way, the anodic layers grown at short and long anodizing time, 15 and 60 min at 0 rpm (Figure 7c,d) show a capacitive behavior as the anodizing time increases at the same time of immersion, being more marked in the spectra at 24 h immersion. The value of the phase angle ranges about 85° from 100 Hz. This result reveals the high stability of the anodic layers grown at both 15 and 60 min of anodizing times.

The Nyquist diagrams of the anodic layers grown at 60 min at 600 rpm, Figure 7e. There is not any significant difference of the stirring speed on the anodizing time for 60 min. However, the impedance modulus in the Bode diagrams of the anodized samples at 600 rpm, Figure 7f, seems to present two time-constants since there is a small change in the slopes on the /Z/ response, which could be associated to the properties of the porous layer and the barrier layer as reported in the literature for anodic layers grown on other metals [54,55].

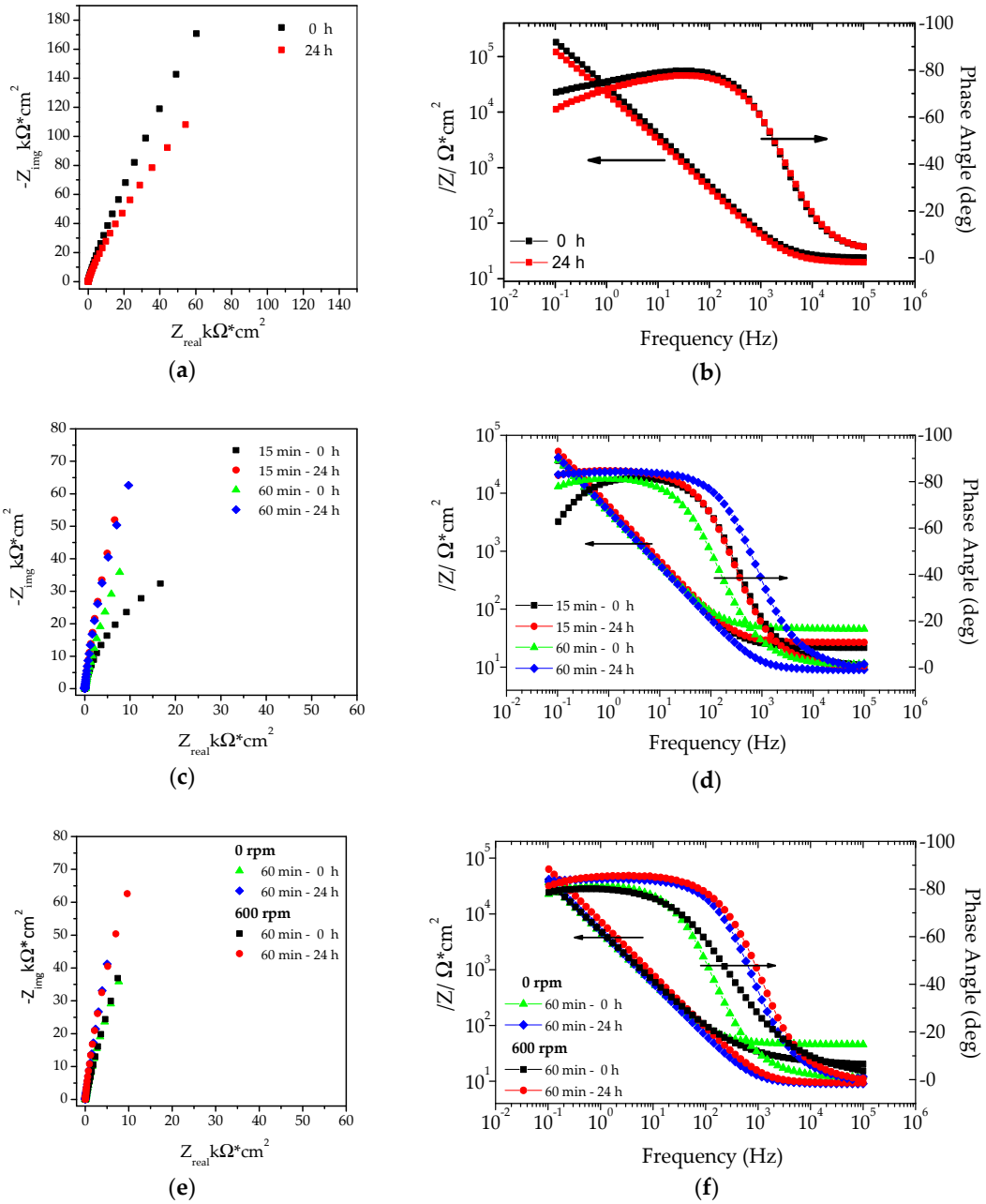

Figure 7. Electrochemical Impedance Spectroscopy (EIS), Nyquist and Bode diagrams at 0 and 24 h of immersion times; (**a**,**b**) corresponding to the non-anodized specimen; (**c**,**d**) anodization treatments at 15 and 60 min a 0 rpm; (**e**,**f**) effect of stirring speeds at 60 min of anodization.

Table 2 summarizes the proposed equivalent electrical circuit used to simulate the behavior of the non-anodized sample, for which an equivalent Randles circuit was used. This equivalent circuit is suitable to model the capacitive behaviour of passive real systems since it allows to model the deviations of the ideal behavior. Where the CPE values obtained, for both immersion times, correspond to the double layer capacitance 30.70 $\mu Ss^{\alpha}/cm^2$ at 0 h and 28.91 $\mu Ss^{\alpha}/cm^2$ at 24 h; while the charge transfer resistance -R_{ct}- presents values of 0.25 MΩ cm^2 and 0.61 MΩ cm^2 at 0 and 24 h immersion respectively, which are typical values for bare 304 SS [56,57].

Table 2. Values of the electrical parameters value of the equivalent circuit used to fit the spectra of the non-anodized specimen.

Circuit Parameter	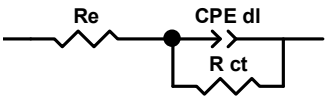	
Immersion time (h)	0	24
R_e (Ω cm^2)	28.06	31.73
CPE_{dl} ($\mu Ss^{\alpha}/cm^2$)	30.76	28.91
α	0.91	0.92
R_{ct} (MΩ cm^2)	0.25	0.61
Chi-sqr (10^{-3})	1.71	1.37

Similarly, to simulate the behavior of the anodic layers grown for 15 min and 60 min at 0 rpm the same equivalent circuit has been used, Table 3. As it can be seen the CPE value decreases with the immersion time in NaCl from 35.96 to 28.96 $\mu Ss^{\alpha}/cm^2$ for the anodic layers grown during 15 min and from 40.79 to 36.23 $\mu Ss^{\alpha}/cm^2$ for the anodic layers grown for 60 min and the values of the charge transfer resistance slightly increase with the immersion time. All, these values are similar to those obtained for the non-anodized sample. These results suggest that the barrier layer of the anodic film shows similar electrochemical properties than the naturally grown oxide layer on 304 SS.

Table 3. Values of the electrical parameter of the equivalent circuit used to fit the spectra of the anodic films for different anodizing times and stirring speeds.

Circuit Parameter	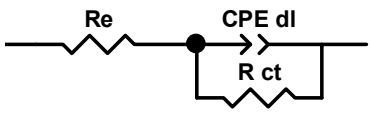				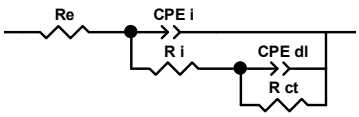 **I Means Anodic Film**	
rpm	0				600	
Immersion time (h)	0		24		0	24
Anodized time (min)	15	60	15	60	60	60
R_e (Ω cm^2)	22.29	46.55	27.02	9.13	21.44	9.45
CPE_{film} ($\mu Ss^{\alpha}/cm^2$)	–	–	–	–	16.83	22.45
α	–	–	–	–	0.89	0.95
$R_{anodic\ layer}$ (Ω cm^2)	–	–	–	–	40.21	240.16
CPE_{dl} ($\mu Ss^{\alpha}/cm^2$)	35.96	40.79	28.96	36.23	23.01	1.37
α	0.92	0.91	0.94	0.94	0.89	1.00
R_{ct} (MΩ cm^2)	0.11	0.68	2.10	2.14	1.09	0.93
Chi-sqr (10^{-3})	1.52	2.10	0.15	0.65	2.63	0.38

Finally, the anodic layers fabricated for 600 rpm were simulated using a circuit equivalent with two time-constants, the first associated with the electrochemical response of the body of anodic layer and the second with the bottom of anodic films.

With CPE values of the anodic layer of 16.83 μSs$^{\alpha}$/cm^2 at 0 h which reaches a value of 22.45 μSs$^{\alpha}$/cm^2 at 24 h of immersion and a load transfer resistance values associated with the body of anodic film of the order of 40.21 Ω cm^2 at 0 h that reaches values of 240 Ω cm^2 at 24 h which are values of the same order of magnitude to those reported by Lucas-Granados et al. [57] in anodic layers grown on iron, where they model the anodic layers they obtain with 3 time counters, where the first two time constants associate them with the morphological characteristics present along the iron nanotubes and the third time constant to the response of the barrier layer which is more compact and much less conductive than the nanostructures body.

The results obtained from the electrochemical impedance are consistent with those found in the polarization curves. All anodic layers reveal similar corrosion kinetics and mechanism than the non-anodized 304 SS, which indicates that the anodizing process does not have detrimental effects on the electrochemical response of the 304 SS.

4. Conclusions

Nano-structured anodic layers are obtained on 304L SS using ethylene glycol + 0.1 mol L^{-1} H_2O + 0.1 mol L^{-1} NH_4F at different stirring speeds and anodizing times. Increasing the stirring speed results in a higher current density-time response and, therefore, in the charge that passes through the system. The increase of the anodizing time favors the growth of an oxide layers with defined nanoporous morphology with pore diameters ~63.0 nm and thicknesses about 1.4 μm. The chemical composition depends on the anodizing time since the mechanisms responsible for the growth of the anodic layer involve ion migration and chemical dissolution. For 45 and 60 min of anodizing a higher content of F and O is found in the outer zone of the anodic layer.

The electrochemical tests confirmed that the responses to corrosion of the oxide layers are independent of the anodizing time and the stirring speed. Moreover, the electrochemical response of all anodic layers grown at different conditions exhibited a similar behavior and do not provide any improvement on the corrosion resistance of the non-anodized 304L SS.

Author Contributions: Conceptualization, M.Á.A.V. and J.M.H.-L.; Methodology, J.M.H.-L.; Investigation, L.P.D.-J. and J.M.H.-L.; Data Curation, L.P.D.-J. and J.M.H.-L.; Writing-Original Draft Preparation, L.P.D.-J. and J.M.H.-L.; Writing-Review & Editing, M.Á.A.V., E.I.C.-G., J.J.R.V., J.J.D.D., A.C.D.C., F.J.R.-V., I.L.A.-L. and J.M.H.-L.; Visualization, L.P.D.-J., E.I.C.-G., J.J.D.D., J.M.H.-L.; Resources, A.C.D.C., M.Á.A.V., J.J.R.V., F.J.R.-V., I.L.A.-L. Supervision, M.Á.A.V. and J.M.H.-L.; Project Administration, J.M.H.-L.; Funding Acquisition, M.Á.A.V. and J.M.H.-L.

Funding: This work was funded by Faculty of Chemical Sciences of the UANL with 02-106939-PST-16-137 project and by the BACTERIA project (MAT2017-86163-C2-1-R), Ministry of Science, Innovation and Universities, SPAIN.

Conflicts of Interest: The autors declare no conflict of interest.

References

1. Jiang, L.; Syed, J.A.; Gao, Y.; Lu, H.; Meng, X. Electrodeposition of Ni $(OH)_2$ reinforced polyaniline coating for corrosion protection of 304 stainless steel. *Appl. Surf. Sci.* **2018**, *440*, 1011–1021. [CrossRef]
2. Cano, E.; Martínez, L.; Simancas, J.; Pérez-Trujillo, F.J.; Gómez, C.; Bastidas, J.M. Influence of N, Ar and Si ion implantation on the passive layer and corrosion behaviour of AISI 304 and 430 stainless steels. *Surf. Coat. Technol.* **2006**, *200*, 5123–5131. [CrossRef]
3. Dadfar, M.; Salehi, M.; Golozar, M.A.; Trasatti, S.; Casaletto, M.P. Surface and corrosion properties of modified passive layer on 304 stainless steel as bipolar plates for PEMFCs. *Int. J. Hydrog. Energy* **2017**, *42*, 25869–25876. [CrossRef]
4. García-Rodríguez, S.; López, A.J.; Torres, B.; Rams, J. 316L stainless steel coatings on ZE41 magnesium alloy using HVOF thermal spray for corrosion protection. *Surf. Coat. Technol.* **2016**, *287*, 9–19. [CrossRef]
5. Habibi, M.; Javadi, S.; Ghoranneviss, M. Investigation on the structural properties and corrosion inhibition of W coatings on stainless steel AISI 304 using PF device. *Surf. Coat. Technol.* **2014**, *254*, 112–120. [CrossRef]

6. Awad, A.M.; Ghazy, E.A.; Abo El-Enin, S.A.; Mahmoud, M.G. Electropolishing of AISI-304 stainless steel for protection against SRB biofilm. *Surf. Coat. Technol.* **2012**, *206*, 3165–3172. [CrossRef]
7. Keller, F.; Hunter, M.S.; Robinson, D.L. Structural features of oxide coatings on aluminum. *J. Electrochem. Soc.* **1953**, *100*, 411–419. [CrossRef]
8. Lee, W.; Park, S.J. Porous anodic aluminum oxide: Anodization and templated synthesis of functional nanostructures. *Chem. Rev.* **2014**, *114*, 7487–7556. [CrossRef]
9. Blawert, C.; Dietzel, W.; Ghali, E.; Song, G. Anodizing treatments for magnesium alloys and their effect on corrosion resistance in various environments. *Adv. Eng. Mater.* **2006**, *8*, 511–533. [CrossRef]
10. Pandey, B.; Thapa, P.S.; Higgins, D.A.; Ito, T. Formation of self-organized nanoporous anodic oxide from metallic gallium. *Langmuir* **2012**, *28*, 13705–13711. [CrossRef]
11. Lee, C.Y.; Lee, K.; Schmuki, P. Anodic formation of self-organized cobalt oxide nanoporous layers. *Angew. Chem.* **2013**, *52*, 2077–2081. [CrossRef] [PubMed]
12. Tsuchiya, H.; Macak, J.M.; Sieber, I.; Taveira, L.; Ghicov, A.; Sirotna, K.; Schmuki, P. Self-organized porous WO_3 formed in NaF electrolytes. *Electrochem. Commun.* **2005**, *7*, 295–298. [CrossRef]
13. Sieber, I.; Hildebrand, H.; Friedrich, A.; Schmuki, P. Formation of self-organized niobium porous oxide on niobium. *Electrochem. Commun.* **2005**, *7*, 97–100. [CrossRef]
14. Zhang, L.; Shao, J.; Han, Y. Enhanced anodization growth of self-organized ZrO_2 nanotubes on nanostructured zirconium. *Surf. Coat. Technol.* **2011**, *205*, 2876–2881. [CrossRef]
15. Zaraska, L.; Gawlak, K.; Gilek, D.; Sulka, G.D. Electrochemical growth of multisegment nanoporous tin oxide layers by applying periodically changed anodizing potential. *Appl. Surf. Sci.* **2018**, *455*, 1005–1009. [CrossRef]
16. Zhou, X.; Nguyen, N.T.; Özkan, S.; Schmuki, P. Anodic TiO_2 nanotube layers: Why does self-organized growth occur—A mini review. *Electrochem. Commun.* **2014**, *46*, 157–162. [CrossRef]
17. Regonini, D.; Satka, A.; Jaroenworaluck, A.; Allsopp, D.W.E.; Bowen, C.R.; Stevens, R. Factors influencing surface morphology of anodized TiO_2 nanotubes. *Electrochim. Acta* **2012**, *74*, 244–253. [CrossRef]
18. Xie, K.; Guo, M.; Huang, H.; Liu, Y. Fabrication of iron oxide nanotube arrays by electrochemical anodization. *Corros. Sci.* **2014**, *88*, 66–75. [CrossRef]
19. Zhang, Z.; Hossain, M.F.; Takahashi, T. Fabrication of shape-controlled α-Fe_2O_3 nanostructures by sonoelectrochemical anodization for visible light photocatalytic application. *Mater. Lett.* **2010**, *64*, 435–438. [CrossRef]
20. Zhang, Z.; Hossain, M.F.; Takahashi, T. Self-assembled hematite (α-Fe_2O_3) nanotube arrays for photoelectrocatalytic degradation of azo dye under simulated solar light irradiation. *Appl. Catal. B Environ.* **2010**, *95*, 423–429. [CrossRef]
21. Xie, K.; Li, J.; Lai, Y.; Lu, W.; Zhang, Z.; Liu, Y.; Zhou, L.; Huang, H. Highly ordered iron oxide nanotube arrays as electrodes for electrochemical energy storage. *Electrochem. Commun.* **2011**, *13*, 657–660. [CrossRef]
22. Jang, J.W.; Park, J.W. Iron oxide nanotube layer fabricated with electrostatic anodization for heterogeneous Fenton like reaction. *J. Hazard. Mater.* **2014**, *273*, 1–6. [CrossRef] [PubMed]
23. Lee, C.Y.; Wang, L.; Kado, Y.; Killian, M.S.; Schmuki, P. Anodic nanotubular/porous hematite photoanode for solar water splitting: Substantial effect of iron substrate purity. *ChemSusChem* **2014**, *7*, 934–940. [CrossRef] [PubMed]
24. Mohapatra, S.K.; John, S.E.; Banerjee, S.; Misra, M. Water photooxidation by smooth and ultrathin α-Fe_2O_3 nanotube arrays. *Chem. Mater.* **2009**, *21*, 3048–3055. [CrossRef]
25. Rangaraju, R.R.; Panday, A.; Raja, K.S.; Misra, M. Nanostructured anodic iron oxide film as photoanode for water oxidation. *J. Phys. D Appl. Phys.* **2009**, *42*, 135303. [CrossRef]
26. Rangaraju, R.R.; Raja, K.S.; Panday, A.; Misra, M. An investigation on room temperature synthesis of vertically oriented arrays of iron oxide nanotubes by anodization of iron. *Electrochim. Acta* **2010**, *55*, 785–793. [CrossRef]
27. Lucas-Granados, B.; Sánchez-Tovar, R.; Fernández-Domene, R.M.; García-Antón, J. Controlled hydrodynamic conditions on the formation of iron oxide nanostructures synthesized by electrochemical anodization: Effect of the electrode rotation speed. *Appl. Surf. Sci.* **2017**, *392*, 503–513. [CrossRef]
28. Deng, H.; Huang, M.-C.; Weng, W.-H.; Lin, J.-C. Photocathodic protection of iron oxide nanotube arrays fabricated on carbon steel. *Surf. Coat. Technol.* **2015**, *266*, 183–187. [CrossRef]

29. Asoh, H.; Nakatani, M.; Ono, S. Fabrication of thick nanoporous oxide films on stainless steel via DC anodization and subsequent biofunctionalization. *Surf. Coat. Technol.* **2016**, *307*, 441–451. [CrossRef]
30. Yang, Y.; Zhou, J.; Detsch, R.; Taccardi, N.; Heise, S.; Virtanen, S.; Boccaccini, A.R. Biodegradable nanostructures: Degradation process and biocompatibility of iron oxide nanostructured arrays. *Mat. Sci. Eng. C Mater.* **2018**, *85*, 203–213. [CrossRef]
31. Prakasam, H.E.; Varghese, O.K.; Paulose, M.; Mor, G.K.; Grimes, C.A. Synthesis and photoelectrochemical properties of nanoporous iron (III) oxide by potentiostatic anodization. *Nanotechnology* **2006**, *17*, 4285–4291. [CrossRef]
32. Zhong, Z.; Qin, J.; Ma, J. Cellulose acetate/hydroxyapatite/chitosan coatings for improved corrosion resistance and bioactivity. *Mat. Sci. Eng. C Mater.* **2015**, *49*, 251–255. [CrossRef] [PubMed]
33. Shayan, M.; Moradi, M.; Plakseychuk, A.Y.; Shankar, R.; Chun, Y. Osteoblast cell response to oxide films formed on nanograin 316L stainless steel obtained by two-dimensional linear plane-strain machining. *Mater. Lett.* **2016**, *177*, 94–98. [CrossRef]
34. Pawlik, A.; Hnida, K.; Socha, R.P.; Wiercigroch, E.; Małek, K.; Sulka, G.D. Effects of anodizing conditions and annealing temperature on the morphology and crystalline structure of anodic oxide layers grown on iron. *Appl. Surf. Sci.* **2017**, *426*, 1084–1093. [CrossRef]
35. Klimas, V.; Pakštas, V.; Vrublevsky, I.; Chernyakova, K.; Jagminas, A. Fabrication and characterization of anodic films onto the type-304 stainless steel in glycerol electrolyte. *J. Phys. Chem. C* **2013**, *117*, 20730–20737. [CrossRef]
36. Albu, S.P.; Ghicov, A.; Schmuki, P. High aspect ratio, self-ordered iron oxide nanopores formed by anodization of Fe in ethylene glycol/NH_4F electrolytes. *Phys. Status Solid* **2009**, *3*, 64–66. [CrossRef]
37. Tsuchiya, H.; Suzumura, T.; Terada, Y.; Fujimoto, S. Formation of self-organized pores on type 316 stainless steel in organic solvents. *Electrochim. Acta* **2012**, *82*, 333–338. [CrossRef]
38. Doff, J.; Archibong, P.E.; Jones, G.; Koroleva, E.V.; Skeldon, P.; Thompson, G.E. Formation and composition of nanoporous films on 316L stainless steel by pulsed polarization. *Electrochim. Acta* **2011**, *56*, 3225–3237. [CrossRef]
39. Kure, K.; Konno, Y.; Tsuji, E.; Skeldon, P.; Thompson, G.E.; Habazaki, H. Formation of self-organized nanoporous anodic films on type 304 stainless steel. *Electrochem. Commun.* **2012**, *21*, 1–4. [CrossRef]
40. Habazaki, H.; Shahzad, K.; Hiraga, T.; Tsuji, E.; Aoki, T. Formation of self-organized porous anodic films on iron and stainless steels. *ECS Trans.* **2015**, *69*, 211–223. [CrossRef]
41. Jagminas, A.; Klimas, V.; Mažeika, K.; Bernotas, N.; Selskis, A.; Niaura, G. Fabrication of thick gel-like films by anodizing iron in a novel electrolyte based on dimethyl sulfoxide and H_2SiF_6. *Electrochim. Acta* **2011**, *56*, 5452–5458. [CrossRef]
42. Shahzad, K.; Tsuji, E.; Aoki, Y.; Nagata, S.; Habazaki, H. Formation and field-assisted dissolution of anodic films on iron in fluoride-containing organic electrolyte. *Electrochim. Acta* **2015**, *151*, 363–369. [CrossRef]
43. Roy, P.; Berger, S.; Schmuki, P. TiO_2 nanotubes: Synthesis and applications. *Angew. Chem.* **2011**, *50*, 2904–2939. [CrossRef] [PubMed]
44. Md Jani, A.M.; Losic, D.; Voelcker, N.H. Nanoporous anodic aluminium oxide: Advances in surface engineering and emerging applications. *Prog. Mater. Sci.* **2013**, *58*, 636–704. [CrossRef]
45. Ghicov, A.; Schmuki, P. Self-ordering electrochemistry: A review on growth and functionality of TiO_2 nanotubes and other self-aligned $MO_{(x)}$ structures. *Chem. Commun.* **2009**, 2791–2808. [CrossRef]
46. Ono, S.; Saito, M.; Asoh, H. Self-ordering of anodic porous alumina formed in organic acid electrolytes. *Electrochim. Acta* **2005**, *51*, 827–833. [CrossRef]
47. Syrek, K.; Kapusta-Kołodziej, J.; Jarosz, M.; Sulka, G.D. Effect of electrolyte agitation on anodic titanium dioxide (ATO) growth and its photoelectrochemical properties. *Electrochim. Acta* **2015**, *180*, 801–810. [CrossRef]
48. Grimes, C.A.; Mor, G.K. *TiO_2 Nanotube Arrays: Synthesis, Properties, and Applications*; Springer: Berlin, Germany, 2009.
49. Habazaki, H.; Konno, Y.; Aoki, Y.; Skeldon, P.; Thompson, G.E. Galvanostatic growth of nanoporous anodic films on iron in ammonium fluoride-ethylene glycol electrolytes with different water contents. *J. Phys. Chem. C* **2010**, *114*, 18853–18859. [CrossRef]

50. Hernández-López, J.M.; Němcová, A.; Zhong, X.L.; Liu, H.; Arenas, M.A.; Haigh, S.J.; Burke, M.G.; Skeldon, P.; Thompson, G.E. Formation of barrier-type anodic films on ZE41 magnesium alloy in a fluoride/glycerol electrolyte. *Electrochim. Acta* **2014**, *138*, 124–131. [CrossRef]
51. Matykina, E.; Hernandez-López, J.M.; Conde, A.; Domingo, C.; de Damborenea, J.J.; Arenas, M.A. Morphologies of nanostructured TiO_2 doped with F on Ti–6Al–4V alloy. *Electrochim. Acta* **2011**, *56*, 2221–2229. [CrossRef]
52. Benoit, M.; Bataillon, C.; Gwinner, B.; Miserque, F.; Orazem, M.E.; Sánchez-Sánchez, C.M.; Tribollet, B.; Vivier, V. Comparison of different methods for measuring the passive film thickness on metals. *Electrochim. Acta* **2016**, *201*, 340–347. [CrossRef]
53. Kondo, M.; Suzuki, N.; Nakajima, Y.; Tanaka, T.; Muroga, T. Electrochemical impedance spectroscopy on in-situ analysis of oxide layer formation in liquid metal. *Fusion Eng. Des.* **2014**, *89*, 1201–1208. [CrossRef]
54. Hernández-López, J.M.; Conde, A.; de Damborenea, J.J.; Arenas, M.A. Correlation of the nanostructure of the anodic layers fabricated on Ti13Nb13Zr with the electrochemical impedance response. *Corros. Sci.* **2015**, *94*, 61–69. [CrossRef]
55. Pan, J.; Thierry, D.; Leygraf, C. Electrochemical impedance spectroscopy study of the passive oxide film on titanium for implant application. *Electrochim. Acta* **1996**, *41*, 1143–1153. [CrossRef]
56. Lv, J.; Luo, H. Comparison of corrosion behavior between coarse grained and nano/ultrafine grained 304 stainless steel by EWF, XPS and EIS. *J. Nucl. Mater.* **2014**, *452*, 469–473. [CrossRef]
57. Lucas-Granados, B.; Sánchez-Tovar, R.; Fernández-Domene, R.M.; García-Antón, J. Iron oxide nanostructures for photoelectrochemical applications: Effect of applied potential during Fe anodization. *J. Ind. Eng. Chem.* **2019**, *70*, 234–242. [CrossRef]